






Distorted-toroidal Flux Rope Model

Teresa Nieves-Chinchilla¹ , Miguel Angel Hidalgo² , and Hebe Cremades³ ¹ Heliospheric Physics Laboratory, Heliophysics Science Division, NASA Goddard Space Flight Center, 8800 Greenbelt Rd., Greenbelt, MD 20770, USA
Teresa.Nieves@nasa.gov² Department of Physics and Mathematics, University of Alcalá Madrid, Spain³ Grupo de Estudios en Heliofísica de Mendoza, CONICET, Universidad de Mendoza, 665 Boulogne Sur Mer, Mendoza 5500, Argentina

Received 2021 August 30; revised 2023 January 4; accepted 2023 January 12; published 2023 April 25

Abstract

The 3D characterization of magnetic flux ropes observed in the heliosphere has been a challenging task for decades. This is mainly due to the limitations on inferring the 3D global topology and physical properties from the 1D time series from any spacecraft. To advance our understanding of magnetic flux ropes whose configuration departs from the typical stiff geometries, here we present an analytical solution for a 3D flux rope model with an arbitrary cross section and a toroidal global shape. This constitutes the next level of complexity following the elliptic-cylindrical (EC) geometry. The mathematical framework was established by Nieves-Chinchilla et al. with the EC flux rope model, which describes a magnetic topology with an elliptical cross section as a first approach to changes in the cross section. In the distorted-toroidal flux rope model, the cross section is described by a general function. The model is completely described by a nonorthogonal geometry and the Maxwell equations can be consistently solved to obtain the magnetic field and relevant physical quantities. As a proof of concept, this model is generalized in terms of the radial dependence of current density components. The last part of this paper is dedicated to a specific function, $F(\varphi) = \delta(1 - \lambda \cos \varphi)$, to illustrate possibilities of the model. This model paves the way toward the investigation of complex distortions of magnetic structures in the solar wind. Future investigations will explore these distortions in depth by analyzing specific events; studying implications for physical quantities, such as magnetic fluxes, helicity, or energy; and evaluating the force balance with the ambient solar wind that allows such distortions.

Unified Astronomy Thesaurus concepts: [Solar wind \(1534\)](#); [Solar coronal mass ejections \(310\)](#); [Solar evolution \(1492\)](#)

1. Introduction

In heliophysics, a flux rope could be defined as a magnetized plasma confined within magnetic field lines wrapping around an axis that transports mass, magnetic flux, energy, and helicity away from the Sun. In an effort to create an unidealized picture of a flux rope in the heliosphere, it could be described by an internal complex current density distribution driving a twisted but not necessarily ordered magnetic field topology that keeps the plasma enclosed. In this description, the global geometry would be determined by the flux rope genesis back at the Sun as well as by the dynamical balance with the ambient solar wind as the flux rope evolves in the heliosphere.

Little is known about the internal structure and global shape of heliospheric flux ropes, basically because of the lack of observations, which are limited to a few locations in the heliosphere. The progressive increase in the number of space-based telescopes, such as the Parker Solar Probe (Fox et al. 2016) and Solar Orbiter (Müller et al. 2020), that build on the work of the Solar and Heliospheric Observatory (Domingo et al. 1995), STEREO (Kaiser et al. 2008), and the Solar Dynamics Observatory (Pesnell et al. 2012) is providing a valuable combination of remote-sensing observations that partially enable us to untangle the third dimension from the ecliptic-based field of view.

On the basis of in situ observations, magnetic flux ropes observed in the heliosphere have been assumed for decades to be

force-free magnetic structures with a simple circular-cylindrical (CC) geometry (Lundquist 1951; Burlaga et al. 1981; Suess 1988; Lepping et al. 1990) and occasionally in magnetohydrostatic force balance (Sonnerup & Guo 1996; Hau & Sonnerup 1999; Hidalgo et al. 2002a, 2002b; Hu 2017). In an effort to reconcile this view with remote-sensing observations, a realistic flux rope may depart from that idealized picture as it propagates through the corona and in the interplanetary medium. The current understanding of observed patterns in these observations suggests that the dark, round void outlined by excess brightness is the flux rope cavity with its axis seen oriented along the line of sight, while the bright front defines the leading edge associated with part of the sheath in interplanetary in situ data (e.g., Rouillard 2011; Kilpua et al. 2017).

The upcoming out-of-the-ecliptic observations from Solar Orbiter are promising with regard to unraveling the global shape of large structures in the inner heliosphere. In parallel with the increase of available observations, the understanding of the fundamental physics associated with flux ropes also requires models adapted to the complexity of the space environment. We approach this challenge with the revision of the CC model in Nieves-Chinchilla et al. (2016), which provides complexity in the flux rope magnetic structure by including the polynomial series in the current density. In a second paper (Nieves-Chinchilla et al. 2018a), we developed a mathematical formulation to solve any magnetohydrodynamic equations in a nonorthogonal coordinate system, and approached the geometrical complexity with an elliptical cross section for the cylinder as an approximation to a distorted flux rope (henceforth the elliptic-cylindrical (EC) model).

This paper aims to advance the development of a model that better converges to the above definition of a heliospheric flux



Original content from this work may be used under the terms of the [Creative Commons Attribution 4.0 licence](#). Any further distribution of this work must maintain attribution to the author(s) and the title of the work, journal citation and DOI.

rope, namely one described by an internal complex current density distribution driving a twisted but not necessarily ordered magnetic field topology. To that aim, we develop a 3D flux rope model based on a toroid but allowing more complex cross section geometries. Section 2 includes the mathematical details of a general model and the physical quantities such as magnetic fluxes, energy, helicity, and Lorentz force. In Section 3, we adapt the model to a specific cross section and compare it with imaging observations with the cylindrical case. Section 4 includes a brief discussion and final remarks.

2. General Distorted-toroidal Flux Rope Model

Following the path of previous papers and assuming a toroidal geometry, we introduce a distorted-toroidal (DT) coordinate system here,

$$\begin{aligned} x &= [\rho + rF \cos \varphi] \cos \psi \\ y &= [\rho + rF \cos \varphi] \sin \psi \\ z &= r \sin \varphi \end{aligned} \quad (1)$$

where ρ is the major radius for the torus, φ and ψ are the poloidal and toroidal angles, and $F = F(\varphi)$ is a function that geometrically characterizes the cross section distortion.

Figure 1 illustrates the global 3D geometry and the details of the distorted (green color) and nondistorted (gray color) cross sections of a uniform-twist magnetic flux rope based on this coordinate system. The new coordinates are indicated in pink color in the graphics. The ψ and φ range from 0 to 2π and the r -coordinate ranges from 0 to R . The r -coordinate is not the distance to the center of the flux rope, which will be defined by the $rF(\varphi)$ function and will shape the cross section. In the case of Figure 1, we have selected the function $F = \delta(1 - \lambda \cos \varphi)$ with $\delta = 0.9$ and $\lambda = 0.4$. In this case, the structure is highly compressed in the outer edge of the torus but it extends beyond the $r = R$ value at the inner edge of the torus. The amount of front compression or rear extension in this case is determined by the λ parameter, while the distortion is defined by the δ parameter. In the more general case, the F function may be generalized to any angular function, depending on the poloidal angle φ and on the number of parameters needed to characterize the cross section.

Figure 2 illustrates some other possibilities of the DT coordinate system for four F functions. In the four cases, colored cross sections are shown in contrast with a semitransparent circular cross section ($F = 1$). Figures 2(a) and (b) illustrate the previously discussed cases for $F = \delta$ and $F = \delta(1 - \lambda \cos \varphi)$. In the latter case, the change in signs of the λ parameter will determine the distortion face, outward for a negative sign, inward for a positive sign. The other two examples, Figures 2(c) and (d), represent two other observed shapes that may recall some white light observations of coronal mass ejections (CMEs) in the heliosphere.

2.1. Model Framework

Since the DT coordinate system is not necessarily orthogonal, any physical quantity should be described by a set of *covariant* and *contravariant* components. Here, we will follow the methodology described in Nieves-Chinchilla et al. (2018a), providing a critical description for this paper.

The basis vectors will be defined as

$$\begin{aligned} \epsilon_r &= [F \cos \varphi \cos \psi, F \cos \varphi \sin \psi, \sin \varphi] \\ \epsilon_\psi &= [-[\rho + rF \cos \varphi] \sin \psi, [\rho + rF \cos \varphi] \cos \psi, 0] \\ \epsilon_\varphi &= r[\mathcal{J} \cos \psi, \mathcal{J} \sin \psi, \cos \varphi] \end{aligned} \quad (2)$$

where

$$\mathcal{J} = \mathcal{J}(\varphi) = F' \cos \varphi - F \sin \varphi, \quad (3)$$

$$F' = \partial_\varphi F. \quad (4)$$

These basis vectors are related to the unit vectors by the scale factors

$$\begin{aligned} h_r &= [F^2 \cos^2 \varphi + \sin^2 \varphi]^{1/2} \\ h_\psi &= (\rho + rF \cos \varphi) \\ h_\varphi &= r[\mathcal{J}^2 + \cos^2 \varphi]^{1/2} = rh \end{aligned} \quad (5)$$

where, for analogy with the EC model, the metric tensor element h_φ is renamed rh .

The metric tensor must be built to relate the covariant (subscript) and contravariant (superscript) spaces. The elements of the metric tensor are

$$g_{rr} = \epsilon_r \cdot \epsilon_r = [F^2 \cos^2 \varphi + \sin^2 \varphi], \quad (6)$$

$$g_{\psi\psi} = \epsilon_\psi \cdot \epsilon_\psi = [\rho + rF \cos \varphi]^2 = h_\psi^2, \quad (7)$$

$$g_{\varphi\varphi} = \epsilon_\varphi \cdot \epsilon_\varphi = r^2[\mathcal{J}^2 + \cos^2 \varphi] = r^2 h^2, \quad (8)$$

$$g_{r\psi} = g_{\psi r} = \epsilon_r \cdot \epsilon_\psi = 0, \quad (9)$$

$$g_{r\varphi} = g_{\varphi r} = \epsilon_r \cdot \epsilon_\varphi = r \cos \varphi [\mathcal{J}F + \sin \varphi] = r \bar{g}_{r\varphi}, \quad (10)$$

$$g_{\psi\varphi} = g_{\varphi\psi} = \epsilon_\psi \cdot \epsilon_\varphi = 0. \quad (11)$$

Note we have renamed $g_{r\varphi} = r \bar{g}_{r\varphi}$ to separate the radial and the angular dependency.

The metric is then

$$\begin{aligned} g^{1/2} &= [g_{rr} g_{\psi\psi} g_{\varphi\varphi} - g_{r\varphi}^2 g_{\psi\psi}]^{1/2} \\ &= r(\rho + rF \cos \varphi) [F \cos^2 \varphi - \mathcal{J} \sin \varphi] = rh_\psi \bar{g}. \end{aligned} \quad (12)$$

Note also that for the cylindrical approximation, $h_\psi = 1$ and $\bar{g} = \delta$ (EC model) or 1 (CC model).

The contravariant components of the metric are

$$g^{rr} = \frac{g_{\psi\psi} g_{\varphi\varphi}}{g} = \frac{h^2}{\bar{g}} \quad (13)$$

$$g^{\psi\psi} = \frac{g_{rr} g_{\varphi\varphi} - g_{r\varphi}^2}{g} = \frac{1}{h_\psi} \quad (14)$$

$$g^{\varphi\varphi} = \frac{g_{rr} g_{\psi\psi}}{g} = \frac{h}{r^2 \bar{g}} \quad (15)$$

$$g^{r\varphi} = g^{\varphi r} = -\frac{g_{r\varphi} g_{\psi\psi}}{g} = -\frac{\bar{g}_{r\varphi}}{r \bar{g}}. \quad (16)$$

The final step is to define operators that allow us to solve the MHD equations and obtain the physical quantities that characterize heliospheric flux ropes (see Nieves-Chinchilla et al. 2018a for more details). The *divergence* of the magnetic field is given by

$$\nabla \cdot \mathbf{B} = \frac{1}{g^{1/2}} \frac{\partial}{\partial q^k} (g^{1/2} B_c^k) \quad (17)$$

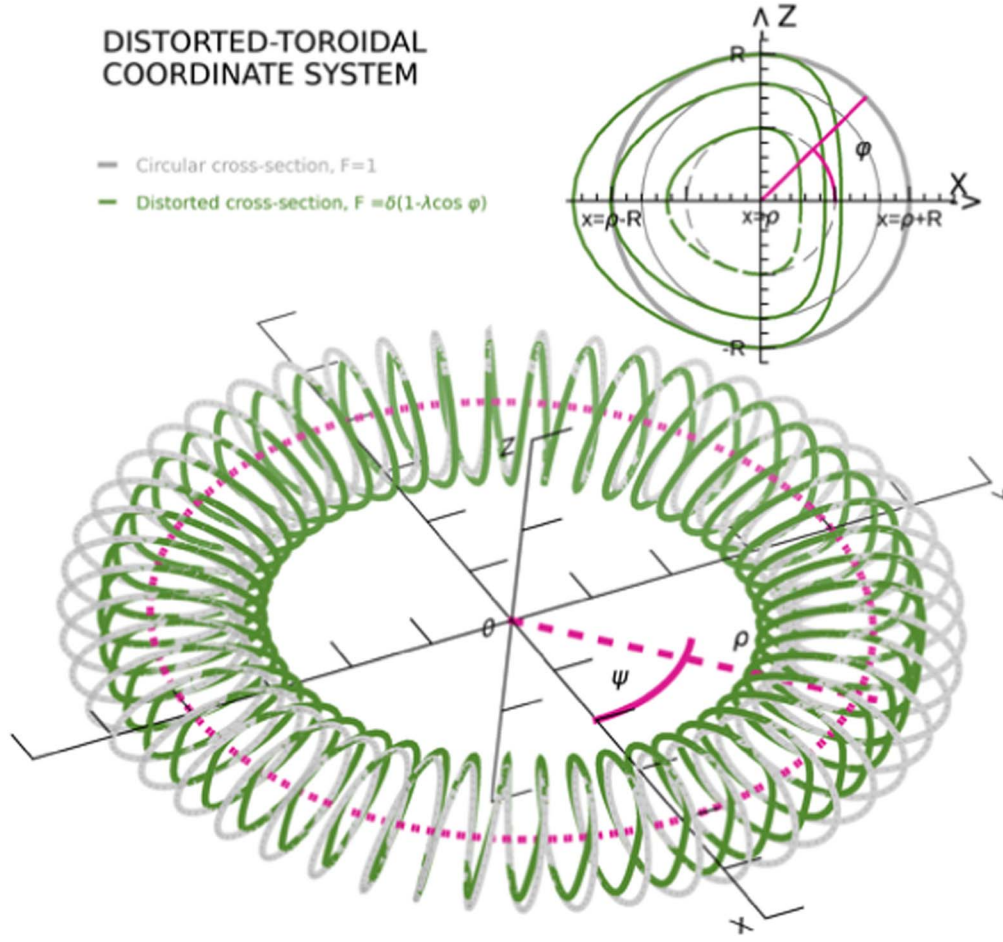


Figure 1. Representation of a circular-toroidal flux rope (gray line) and a distorted flux rope with a uniform-twist field. In pink color are shown the r -, ψ -, and φ -components: ρ , the major radius; R , the minor radius; ψ , the azimuth angle; and φ , the poloidal angle. Both structures are represented in the same DT coordinate system with $F = 1$ (gray color, for the circular case) or $F = \delta(1 - \lambda \cos \varphi)$ (green color, for the distorted case), $\rho = 4$, $\delta = 0.9$, and $\lambda = 0.4$.

where B_c^k denotes the nonscaled contravariant components of the magnetic field, and $q^k = (r, \psi, \varphi)$. The same equation is used for the current density ($\nabla \cdot \vec{j} = 0$).

The curl components for the magnetic field are given by

$$(\nabla \times \mathbf{B})^i = \frac{1}{g^{1/2}} \varepsilon^{ijk} \frac{\partial}{\partial q^j} (g_{kl} B_c^l) \quad (18)$$

where ε^{ijk} denotes the Levi-Civita coefficients.

Assuming $(0, B_c^\psi, B_c^\varphi)$ and $(j_c^r, j_c^\psi, j_c^\varphi)$ vector components of the magnetic field and current density, the equations to solve are obtained from Ampere's law and Gauss's law for magnetism for a stationary case and imposing the continuity equation for the currents. Based on the geometry, with the same cross section shape and size along the flux rope axis, $B_c^r = 0$, and assuming the same twisting profile, $d/d\psi = 0$. Thus, the equation system will be

$$\partial_\varphi (g^{1/2} B_c^\varphi) = 0, \quad (19)$$

$$\partial_\varphi (g_{\psi\psi} B_c^\psi) = -g^{1/2} \mu_0 j_c^r, \quad (20)$$

$$\partial_\varphi (g_{r\varphi} B_c^\varphi) - \partial_r (g_{\varphi\varphi} B_c^\varphi) = g^{1/2} \mu_0 j_c^\psi, \quad (21)$$

$$\partial_r (g_{\psi\psi} B_c^\psi) = g^{1/2} \mu_0 j_c^\varphi, \quad (22)$$

$$\partial_r (g^{1/2} j_c^r) + \partial_\varphi (g^{1/2} j_c^\varphi) = 0. \quad (23)$$

Here the magnetic field and current density components are the nonscaled contravariant coefficients of ε_i and they should be scaled using the scale factors of Equation (5).

Then, directly from Equation (19), the solution for the poloidal magnetic field component must be

$$B_c^\varphi(r, \varphi) = \frac{\bar{B}_c^\varphi(r)}{h_\psi \bar{g}} \quad (24)$$

where henceforth $\bar{B}_c^\varphi = \bar{B}_c^\varphi(r)$.

Now solving for B_c^φ in Equation (21), we obtain

$$\partial_r (\bar{B}_c^\varphi) + \left[\frac{1}{r} \chi(\varphi) - \frac{F \cos \varphi}{h_\psi} \sigma(\varphi) \right] \bar{B}_c^\varphi = -\mu_0 \frac{h_\psi^2 \bar{g}^2}{r h^2} j_c^\psi, \quad (25)$$

with

$$\chi(\varphi) = 2 - \frac{\partial_\varphi \bar{g}_{r\varphi}}{h^2} + \frac{\bar{g}_{r\varphi} \partial_\varphi \bar{g}}{\bar{g} h^2} \quad (26)$$

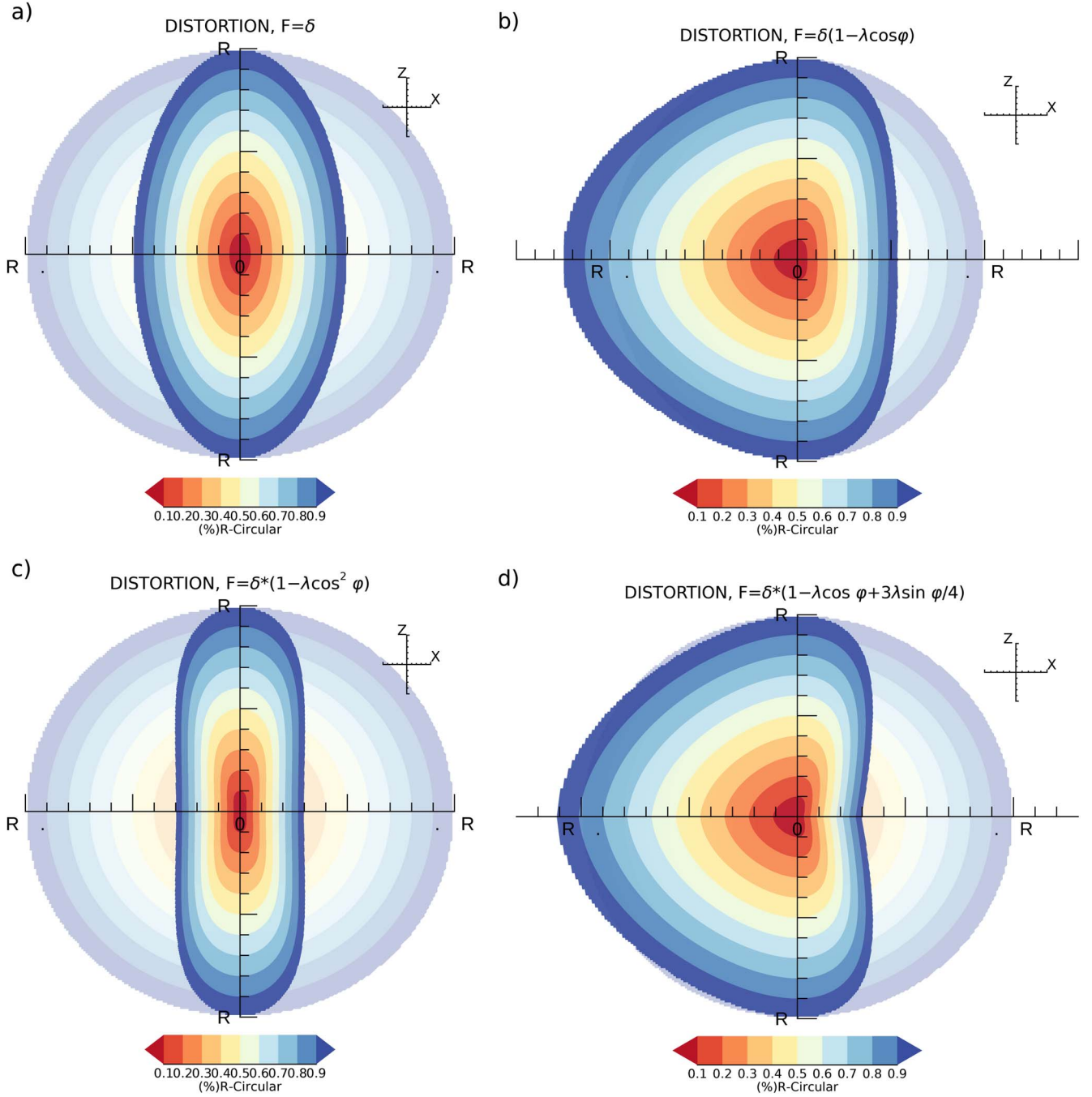


Figure 2. Illustration of different cross sections based on (a) $F = \delta$ (elliptical cross section), (b) $F = \delta(1 - \lambda \cos \varphi)$ with $\delta = 0.9$ and $\lambda = 0.4$, (c) $F = \delta(1 - \lambda \cos^2 \varphi)$ with $\delta = 0.5$ and $\lambda = 0.4$, and (d) $F = \delta(1 - \lambda \cos \varphi + 3\lambda \sin \varphi/4)$ with $\delta = 0.9$ and $\lambda = 0.4$. In all simulations, $\rho = 3R$. Each case is displayed on top of a semitransparent circular cross section to highlight the distortion.

$$\sigma(\varphi) = 1 + \frac{\bar{g}_{r\varphi}}{h^2} \frac{\mathfrak{J}}{F \cos \varphi}. \quad (27)$$

The solution to the equation is

$$\bar{B}_c^\varphi = -\mu_0 \frac{h_\psi^\sigma \bar{g}^2}{r^\chi h^2} \int_0^r \frac{r'^{\chi-1}}{h_\psi^{\sigma-2} j_c^\psi(r, \varphi)} dr', \quad (28)$$

where $j_c^\psi(r, \varphi)$ should be such that $\bar{B}_c^\varphi(r)$ does not depend on the poloidal coordinate. Thus,

$$\begin{aligned} j_c^\psi(r, \varphi) &= \frac{h^2 h_\psi^{\sigma-2}}{\bar{g}^2 r^{\chi-1}} \partial_r \left[\frac{r^\chi}{h_\psi^\sigma} k(r) \right] \\ &= \frac{h^2}{\bar{g}^2 h_\psi^2} \left[k(r) \left(\chi - \frac{r}{h_\psi} \sigma \right) + k'(r) r \right], \end{aligned} \quad (29)$$

where $k(r)$ is an arbitrary function solely dependent on r . The nonscaled poloidal magnetic field component is

$$B_c^\varphi = \frac{\bar{B}_c^\varphi}{h_\psi \bar{g}} = -\mu_0 \frac{k(r)}{h_\psi \bar{g}}. \quad (30)$$

Now solving, from Equation (23), the poloidal current density component, we obtain

$$j_c^\varphi = \frac{\partial_r(rf(r))}{r\bar{g}}, \quad (31)$$

and the radial current density component is

$$j_c^r = -\frac{\mathfrak{J}}{h_\psi \bar{g}} f(r). \quad (32)$$

Note that, in the particular case of $F(\varphi) = \text{constant}$ and a cylindrical geometry, $j^r=0$ would be a solution of the equations. This was the solution expressed in the case of the EC and CC models.

Now, to solve for the toroidal magnetic field component, we can impose $B_c^\psi(r, \varphi) = \frac{\bar{B}_c^\psi(r)}{h_\psi}$, and then the scaled toroidal magnetic field component will be

$$\bar{B}_c^\psi(r) = -\mu_0 f(r) |'_0, \quad (33)$$

where we will impose that the value of the central magnetic field decreases with the radial distance to reach a value at $r=R$ that may be canceled or a scaled value of the central magnetic field. This boundary condition may be arbitrarily set. We will rename this function

$$f_r(r) = f(r) |'_0. \quad (34)$$

Then, the nonscaled toroidal magnetic field component is

$$B_c^\psi = -\mu_0 \frac{1}{h_\psi} f_r(r) \Big|_0^r. \quad (35)$$

The scaled magnetic field components are

$$\begin{aligned} B^r(r, \varphi) &= 0 \\ B^\psi(r, \varphi) &= h_\psi B_c^\psi(r, \varphi) = -\mu_0 [f_r(r) |'_0] \\ B^\varphi(r, \varphi) &= r h B_c^\varphi(r, \varphi) = -\mu_0 \frac{h}{h_\psi \bar{g}} r k(r). \end{aligned} \quad (36)$$

The scaled current density components are

$$\begin{aligned} j^r(r, \varphi) &= -h_r j_c^r(r, \varphi) = -\frac{h_r \mathfrak{J}}{\bar{g} h_\psi} f(r) \\ j^\psi(r, \varphi) &= h_\psi j_c^\psi(r, \varphi) = \frac{h^2}{\bar{g}^2 h_\psi} \left[k(r) \left(\chi - \frac{r}{h_\psi} \sigma \right) + k'(r) r \right], \\ j^\varphi(r, \varphi) &= r h j_c^\varphi(r, \varphi) = h \frac{\partial_r(rf(r))}{\bar{g}}. \end{aligned} \quad (37)$$

The set of Equations (36) and (37) are the general solution of the magnetic field for the radial profile of the current density components. Table 1 summarizes the geometrical factors and parameterized equations that directly impact the above model equations. Thus, for any geometry consistent with the

Table 1
Geometrical Factors, including Scale Factors and Metric, and Parameterized Equations Needed to Build the Model Equations

	Geometrical Factors and Parametric Funct.
1.	$\mathfrak{J}(\varphi) = F' \cos \varphi - F \sin \varphi$
2.	$h_r = [F^2 \cos^2 \varphi + \sin^2 \varphi]^{1/2}$
3.	$h = [\mathfrak{J}^2(\varphi) + \cos^2 \varphi]^{1/2}$
4.	$h_\psi = (\rho + rF \cos \varphi)$
5.	$\bar{g} = [F \cos^2 \varphi - \mathfrak{J} \sin \varphi]$
6.	$\bar{g}_{r\varphi} = \cos \varphi [\mathfrak{J} F + \sin \varphi]$
7.	$\chi(\varphi) = 2 - \frac{\partial_\varphi \bar{g}_{r\varphi}}{h^2} + \frac{\bar{g}_{r\varphi} \partial_\varphi \bar{g}}{\bar{g} h^2}$
8.	$\sigma(\varphi) = 1 + \frac{\bar{g}_{r\varphi} \mathfrak{J}}{h^2 F \cos \varphi}$

coordinate system, Equation (1), and a chosen radial profile of the current density component, the solution can be found.

For completeness and consistency with the CC and EC models, relevant physical quantities such as magnetic fluxes, magnetic energy, and helicity have been developed in the [Appendix](#). The analysis will be carried out in forthcoming studies.

2.2. A General Case of Radial Variation of the Current Density Components

In agreement with previous papers, the current density components could be selected using the radial polynomial function with arbitrary coefficients. Here, we are going to simplify the problem and select one series term to develop the problem. Thus,

$$k(r) = \beta_m r^m, \quad \text{with } m \geq 0, \quad (38)$$

$$f(r) = -\alpha_n r^{n+1}, \quad \text{with } n \geq 1, \quad (39)$$

where α_n and β_m are the two coefficient parameters of the model, and the m and n indices determine the radial profile of the current density components and eventually the magnetic field.

The scaled current density components are

$$\begin{aligned} j^r(r, \varphi) &= h_r \frac{\mathfrak{J}}{h_\psi \bar{g}} \alpha_n r^{n+1}, \\ j^\psi(r, \varphi) &= \frac{h^2 h_\psi}{\bar{g}^2} \beta_m r^m \left[\chi + m - \frac{r}{h_\psi} \sigma \right], \\ j^\varphi(r, \varphi) &= -\frac{h}{\bar{g}} (n+1) \alpha_n r^n. \end{aligned} \quad (40)$$

The scaled magnetic field components are

$$\begin{aligned} B^r(r, \varphi) &= 0 \\ B^\psi(r, \varphi) &= \mu_0 \alpha_n [\tau R^{n+1} - r^{n+1}] \\ B^\varphi(r, \varphi) &= -\frac{h}{h_\psi \bar{g}} \beta_m r^{m+1}. \end{aligned} \quad (41)$$

The above equations could be simplified to a single term of the polynomial series and parameterized to the parameters

Table 2

Functions, Scale Factors, Parametric Functions, and Magnetic Field Model Equations Associated with the Geometries Depicted in Figure 2

Geometry	Factors	Field
Circular	$F = 1$	
	$F' = 0$	$B^r = 0$
	$\mathcal{J} = -\sin \varphi$	$B^\psi = B_n[\tau - \bar{r}^{n+1}]$
	$h_r = h = \bar{g} = 1$	$B^\varphi = -\frac{1}{h_\psi} \frac{B_n}{C_{nm}} \bar{r}^{m+1}$
	$h_\psi = (\rho + r \cos \varphi)$	
Elliptic [Figure 2(a)]	$F = \delta$	
	$F' = 0$	$B^r = 0$
	$\mathcal{J} = -\delta \sin \varphi$	$B^\psi = B_n[\tau - \bar{r}^{n+1}]$
	$h_r = [\sin^2 \varphi + \delta^2 \cos^2 \varphi]^{1/2}$	$B^\varphi = -\frac{h}{\delta h_\psi} \frac{B_n}{C_{nm}} \bar{r}^{m+1}$
	$h = [\delta^2 \sin^2 \varphi + \cos^2 \varphi]^{1/2}$	
	$\bar{g} = \delta$	
	$h_\psi = (\rho + r \delta \cos \varphi)$	
$g_{r\varphi} = r(1 - \delta^2) \sin \varphi \cos \varphi$		
Distorted [Figure 2(b)]	$F = \delta(1 \pm \lambda \cos \varphi)$	
	$F' = \mp \delta \lambda \sin \varphi$	$B^r = 0$
	$\mathcal{J} = -\delta \sin \varphi [1 \pm 2\lambda \cos \varphi]$	$B^\psi = B_n[\tau - \bar{r}^{n+1}]$
	(see Table 1 for h_r, h, \bar{g}, h_ψ)	$B^\varphi = -\frac{h}{\bar{g} h_\psi} \frac{B_n}{C_{nm}} \bar{r}^{m+1}$
Distorted [Figure 2(c)]	$F = \delta(1 \pm \lambda \cos^2 \varphi)$	
	$F' = \mp 2\delta \lambda \sin \varphi \cos \varphi$	$B^r = 0$
	$\mathcal{J} = -\delta \sin \varphi [1 \pm 3\lambda \cos^2 \varphi]$	$B^\psi = B_n[\tau - \bar{r}^{n+1}]$
	(see Table 1 for h_r, h, \bar{g}, h_ψ)	$B^\varphi = -\frac{h}{\bar{g} h_\psi} \frac{B_n}{C_{nm}} \bar{r}^{m+1}$

$C_{nm} = \frac{\alpha_n}{\beta_m} R^{n-m}$ and $B_n = \mu_0 \frac{\alpha_n}{R^{n+1}}$. Thus, the magnetic field components are

$$B^\psi(r, \varphi) = B_n[\tau - \bar{r}^{n+1}]$$

$$B^\varphi(r, \varphi) = -\frac{h}{h_\psi \bar{g}} \frac{B_n}{C_{nm}} \bar{r}^{m+1}. \quad (42)$$

Table 2 includes all geometrical factors and solutions for the parameterized equations listed in Table 1 for the circular case, the elliptical case, and the distorted cases $F = \delta(1 \pm \lambda \cos \varphi)$ and $F = \delta(1 \pm \lambda \cos^2 \varphi)$. The case of Figure 3(d) brings more complex calculations that can be approached numerically. The same exercise can be done for distortions more complex than those shown in Figure 2.

Figure 3 shows the total magnetic field distribution (first column) and the poloidal (second column) and axial (third column) magnetic field component distribution for the four distorted cross-section cases and in the same order of Figure 2. Figures 3(a)–(c) display the case of $F = \delta$, (d)–(f) correspond to $F = \delta(1 - \lambda \cos \varphi)$, (g)–(i) correspond to $F = \delta(1 - \lambda \cos^2 \varphi)$, and (j)–(l) illustrate the $F = \delta(1 - \lambda \cos \varphi + 3\lambda \sin \varphi/4)$ example. Each case is displayed on top of the corresponding quantity for the circular cross-section distribution in the semitransparent background to highlight the effect of compression in the quantity and distribution over the cross section. In the simulations, we use $\rho = 3R$, $\lambda = 0.4$, and $\delta = 0.5$ in all cases except those in Figures 3(d)–(f), which consider $\delta = 0.9$. In all cases, the torus center is located on the left of each plot. Thus, due to curvature, there is an increase in the left side of the magnetic field intensity in the magnitude or components, more or less depending on the level of the curvature. In general, as the curvature increases, there is a more notable increase of the

intensity of the field. The effect is remarkable in the toroidal magnetic field component and consequently, in the magnitude, but there is no effect in the case of the poloidal component. In the simulated cases here, the effect can be similar to or greater than the compression but more localized. Thus, as the spacecraft crosses the structure, the in situ magnetic field observations should indicate a smooth increase in the compression area but a sharper and sudden increase in the curved area.

However, in real events, the combinations of these effects can be more complicated. Nieves-Chinchilla et al. (2018b) carried out a survey of the interplanetary CMEs (ICMEs) observed by the Wind spacecraft during the first 20 yr of the mission. Based on the analysis of the magnetic field strength profile, the authors proposed several scenarios, depicted in Figure 11 of the paper. For instance, according to the data analysis results, 22% of the observed ICMEs displayed magnetic field strength compression at the back of the structure. The specific case of the event observed on 2000 November 6 (day 311), in Figure 6(c) of that paper, depicts a back compression of the magnetic field strength in spite of the structure showing an expansion velocity $V_{\text{exp}} = 58 \text{ km s}^{-1}$. This may be evidence of the effect of the curvature in the in situ observations. In the case of the asymmetric cross-section distortions addressed here (Figures 3(a)–(c) and Figures 3(g)–(i)), there is a bilateral compression. This effect is also due to the curvature plus the front compression is due to the distortion. The magnetic field profile may result in a symmetric magnetic field strength and it would be difficult to decipher signatures of distortion. Examples of this scenario are the event observed by Wind on 2010 January 1 (see Figures 5 and 9(b) in Nieves-Chinchilla et al. 2016) and the event observed on 2013 June 27 (see Figure 7 in Nieves-Chinchilla et al. 2019).

These are some real-case events where we can interpret signatures of distortion or compression. However, the next section shows more insights for the specific case of $F = \delta(1 \pm \lambda \cos \varphi)$ in a highly curved and cylindrical flux rope structure. This is an exercise of *human* training based on visual inspection in order to move forward in the understanding of the distortion effect in in situ observations. Thus, this preliminary back-and-forth exercise between the observations and models would be a prologue to an exhaustive machine-learning training method (see, for instance, dos Santos et al. 2020; Narock et al. 2022).

3. Magnetic Field Imprints of the Curved–Distorted Flux Rope

As part of this paper, we have carried out a study of the implications of distortion in the magnetic field configuration as observed by spacecraft crossing a flux rope. The goal is to identify what in situ signatures could provide insights into distortion, compression, and curvature before carrying out the traditional fitting of the model to the in situ observations. Thus, the first approach would be to learn from the model to identify such signatures based on visual inspection as part of *human* training. This exercise would be similar but opposite to the study carried out by Nieves-Chinchilla et al. (2018b) that looked for signatures in the ICMEs observed by Wind for 20 yr to identify distortion, expansion, or curvature signatures. In our case, we will simulate the trajectory of a spacecraft to carry out human training based on visual

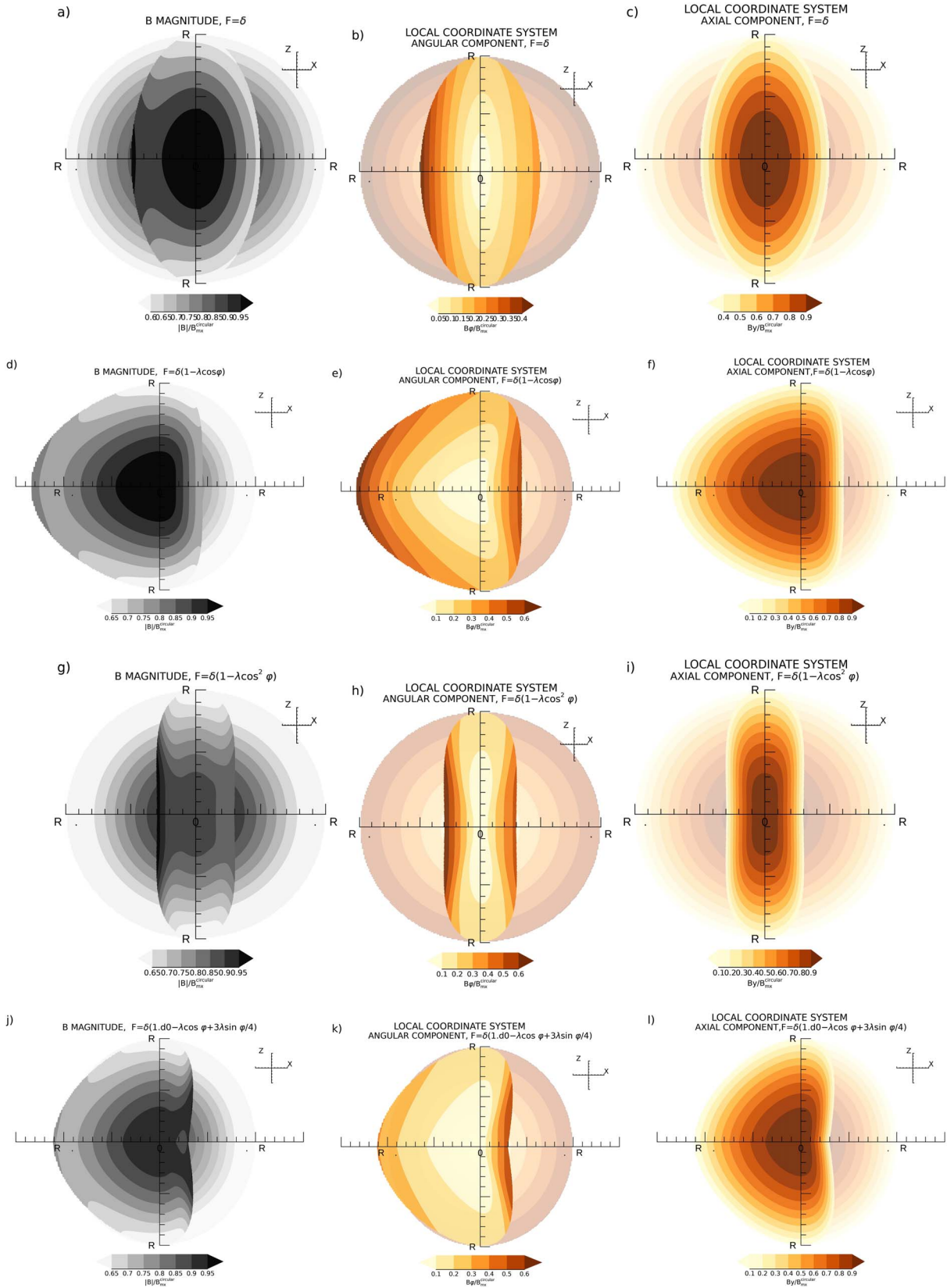


Figure 3. Each column in this array of plots shows the magnetic field magnitude distribution (first column) or the poloidal (second column) or axial (third column) component for the four F functions displayed in Figure 2. From the top (a)–(c) correspond to $F = \delta$ with $\delta = 0.5$ and $\rho = 1.5R$; (d)–(f) correspond to $F = \delta(1 - \lambda \cos \varphi)$ with $\delta = 0.9$, $\lambda = 0.4$, and $\rho = 2R$; (g)–(i) correspond to $F = \delta(1 - \lambda \cos^2 \varphi)$ with $\delta = 0.5$, $\lambda = 0.4$, and $\rho = 2R$; and (j)–(l) correspond to $\delta(1 - \lambda \cos \varphi + 3 \lambda \sin \varphi/4)$ with $\delta = 0.9$ and $\lambda = 0.4$. Each case is displayed on top of the corresponding quantity for the semitransparent circular cross-section distribution to highlight the change due to the distortion. The torus center is located on the left of each plot.

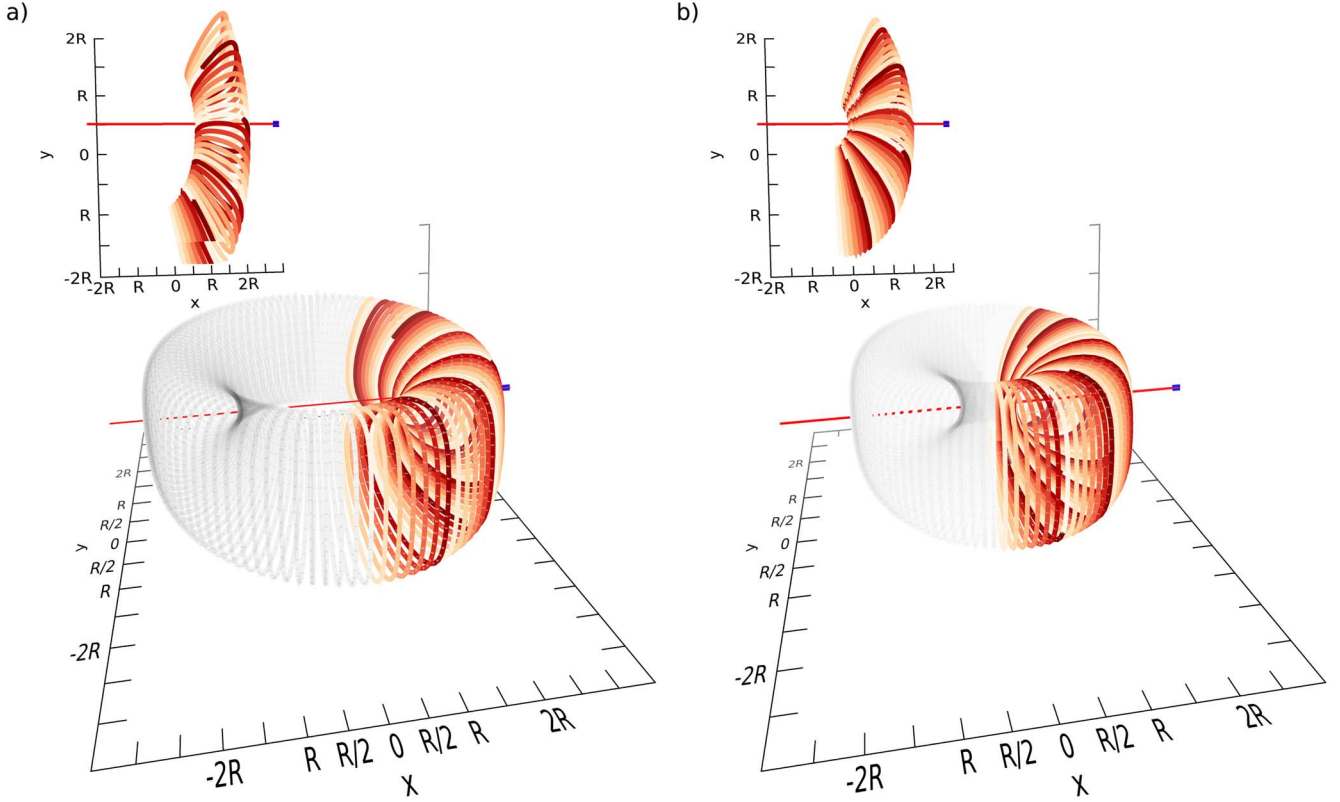


Figure 4. 3D view of the toroidal flux rope based on the geometry $F = \delta(1 - \lambda \cos \varphi)$ for (a) $\rho = 1.5R$ and (b) $\rho = 2.5R$. In both cases, $\delta = 0.8$, and $\lambda = 0.4$. The red line indicates the trajectory of a simulated spacecraft. The blue dots indicate the spacecraft entrance location.

inspection, learn how to identify signatures of distortion or curvature in real data, and adapt the model to these structures before fitting them.

In the following section, we will first define the trajectory of the spacecraft taking into consideration the geometry of the distortion, so as to generate synthetic magnetic field profiles. Then, we will discuss the implications of curvature and distortion in in situ observations of the magnetic field by a satellite. For the experiment we will use one of the functions we discussed in the previous section $F = \delta(1 - \lambda \cos \varphi)$. We will cross two different curvatures and we will map the magnetic field magnitude and components to evaluate deviations from the expected in situ signatures that a magnetometer would record if crossing a cylinder with a circular cross-section geometry. We then will look for such signatures in the real data. This exercise will pave the way toward developing a more sophisticated model to identify such signatures.

3.1. Spacecraft Trajectory

This section is dedicated to evaluating the effect of distortion in 3D reconstructions based on in situ data. The trajectory of the spacecraft is defined by the location of the spacecraft at the entrance of the flux rope as indicated by Nieves-Chinchilla et al. (2018a),

$$x_0 = \frac{v_{sw}(t_t - t_0)}{2} - \frac{F_1}{F_2} z_0. \quad (43)$$

In the case of the simulated spacecraft trajectory, the transit time will be

$$t_s = \frac{2F}{v_{sw}} \frac{\sqrt{R^2 F_2 - y_0^2 F_3^2}}{F_2}, \quad (44)$$

where

$$\begin{aligned} F_1 &= (F^2 - 1) \cos \phi \cos \theta \sin \xi \cos \xi + a \sin \phi \sin \theta \cos \theta \\ F_2 &= b \cos^2 \phi + a \sin^2 \phi \sin^2 \theta + 2(F^2 - 1) \\ &\quad \times \cos \phi \sin \phi \sin \theta \sin \xi \cos \xi, \\ F_3 &= \sqrt{1 - \sin^2 \phi \cos^2 \theta} \end{aligned}$$

and

$$\begin{aligned} a &= [F^2 \cos^2 \xi + \sin^2 \xi] \\ b &= [F^2 \sin^2 \xi + \cos^2 \xi]. \end{aligned} \quad (45)$$

Note that we have corrected here an error in Equation (51) of Nieves-Chinchilla et al. (2018a). In the case of a reconstruction the spacecraft transit time, t_s , and the bulk speed, v_{sw} , are obtained from the observations and the flux rope radius, R , is obtained as a deduced output parameter. In the case of synthetic data, R and v_{sw} are the input parameters, and t_s is the output parameter.

3.2. Implications on Magnetic Field Imprints at a Spacecraft Crossing a Distorted Flux Rope with Different Curvatures and Impact Parameters

In this section, we simulate the spacecraft trajectory and collect the expected magnetic field observations assuming one

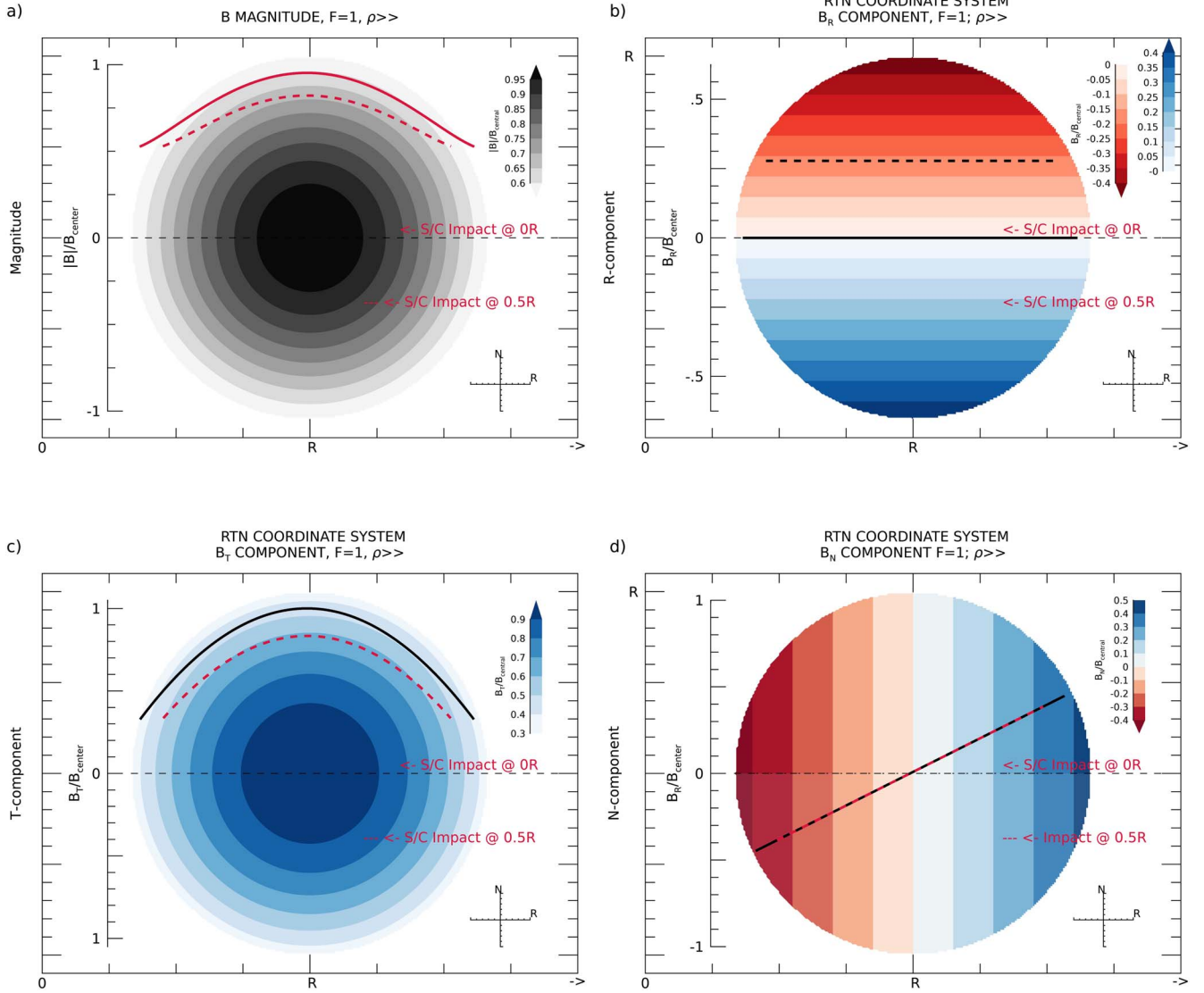


Figure 5. Contour plots of the magnetic field strength and RTN coordinates distributed on the flux rope cross section in the case of a CC cross section with ρ large enough ($\rho \gg 1$) for it to be considered a cylindrical geometry. Overplotted in each contour plot are the magnetic field values measured by a spacecraft crossing through the flux rope center and at a 50% radial distance from the center, $y_0 = 0.5R$ (solid and dashed lines, respectively).

of the geometries described in this paper. The goal is to make an illustration to understand implications and be able to analyze the resultant magnetic field configuration when the structure is crossed by a spacecraft with the flux rope having different curvatures of the axis. For this first experiment, we have selected the m, n pair $[0, 1]$ and $F = \delta(1 - \lambda \cos \varphi)$ to describe the cross-section geometry. The magnetic field model equations are

$$\begin{aligned} B^\psi(r, \varphi) &= B_1[\tau - \bar{r}^2], \\ B^\varphi(r, \varphi) &= -\frac{h}{h_\psi \bar{g}} \frac{B_1}{C_{10}} \bar{r}, \end{aligned} \quad (46)$$

with

$$\begin{aligned} \bar{r} &= \delta \sin \varphi [1 + 2\lambda \cos \varphi], \\ h &= [\delta(1 - \lambda \cos \varphi)^2 \sin^2 \varphi + \cos^2 \varphi]^{1/2}, \\ h_\psi &= (\rho + r\delta(1 - \lambda \cos \varphi) \cos \varphi), \\ \bar{g} &= \delta(1 - \lambda \cos \varphi), \end{aligned} \quad (47)$$

from Table 2. B_1 , C_{10} , and τ are the model parameters and \bar{r} is the normalized cross-section radial distance.

We have considered two toroidal geometries to compare with the cylindrical case. Figure 4 illustrates flux ropes with a central radius of $\rho = 2.5R$ (Figure 4(a)) and $\rho = 1.5R$ (Figure 4(b)), R being the major radius of the cross section. The tori have been partially colored at the front, simulating the front of a CME and indicating the trajectory of the spacecraft in red color with the spacecraft in blue color. The simulated spacecraft crosses through the compressed front of the flux rope and through its center ($y_0 = 0$). On the top left of each figure, we have included the flux rope front projected on the XY -plane to highlight the different curvatures of the two cases and to distinguish the spacecraft trajectory from the flux rope front on a perpendicular path to the axis. The parameters for the simulation are $\delta = 0.8$, $\lambda = 0.4$, $\tau = 1.5$, and $C_{10} = -1.5$ (left-handed).

Thus, to evaluate the effect of distortion as well as of curvature in in situ observations of spacecraft crossing the structure, we have transformed the magnetic field

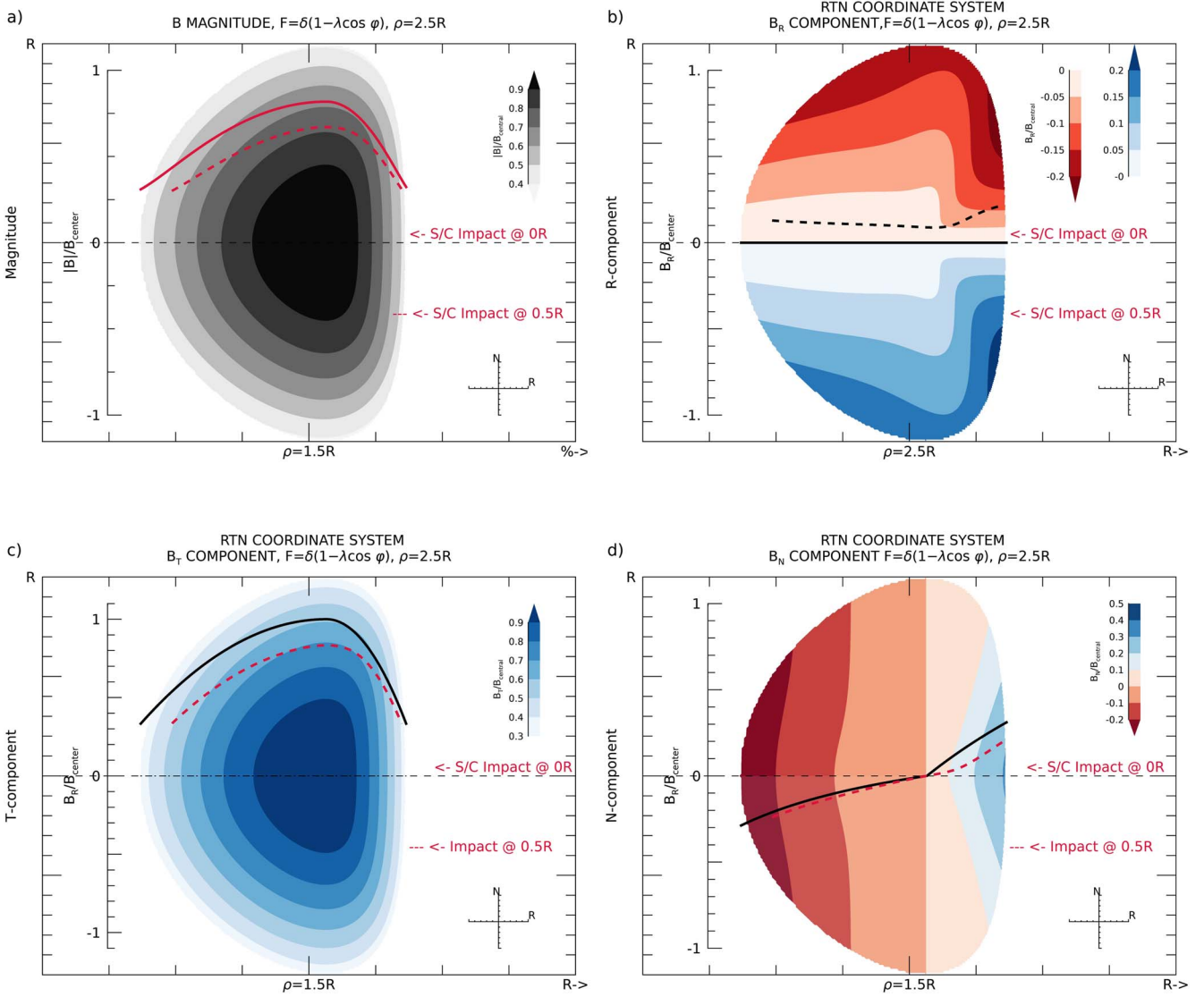


Figure 6. Contour plots of the magnetic field strength and RTN components distributed on the flux rope cross section in the case of a distorted cross section with a geometry of $F = \delta(1 - \lambda \cos \varphi)$ with large $\rho = 2.5R$ (Figure 4(a)). Overplotted in each contour plot are the magnetic field values measured by a spacecraft crossing through the flux rope center and at a 50% radial distance from the center, $y_0 = 0.5R$ (solid and dashed lines, respectively).

components from the local coordinate system to, in this case, the RTN coordinate system. Figures 5, 6, and 7 depict arrays of plots for the two scenarios of Figure 4 plus the case of the CC geometry, which will serve as a reference scenario to compare them with. The figures show the cross-section distribution of the magnetic field strength and RTN components for three different geometries. Figure 5 displays a CC geometry, Figure 6 displays a cross section distorted with low curvature (associated with Figure 4(a), $F = \delta(1 - \lambda \cos \varphi)$ with $\rho = 2.5R$), and Figure 7 displays the same cross-section distortion and high curvature (associated with Figure 4(b), $F = \delta(1 - \lambda \cos \varphi)$ with $\rho = 1.5R$). For each geometry, we have simulated the crossing of a spacecraft from the right side through the center, as illustrated in Figure 4, and overplotted with a solid line the magnetic field strength or components, depending on the case. To evaluate the effect of spacecraft impact distance with respect to the center on the quantities, we have also simulated the crossing of a spacecraft at the closest approach of

$y_0 = 0.5R$, i.e., halfway from the axis to the flux rope edge (dashed lines).

Comparing the magnetic field strength (Figures 5(a), 6(a), and 7(a)), we can observe that the distortion implies an increase of the asymmetry in the contour plot with a compression of the magnetic field at the front of the structure. The curvature also implies an increase of the magnetic field strength. This assessment is confirmed if we analyze the magnetic field configuration observed by the simulated spacecraft magnetometer, the red lines overplotted on the black contour plots. While in the CC case the magnetic configuration is symmetric, in the distorted cases the maximum is displaced toward the front of the flux rope. In the case of the highly curved flux rope, there is a marked increase in the strength as the spacecraft leaves the structure (back side of Figure 7(a)). Note that as we increase the distance of the spacecraft to the center, the maximum of the strength decreases as expected, but it is important to highlight that also the effect of the curvature is less relevant.

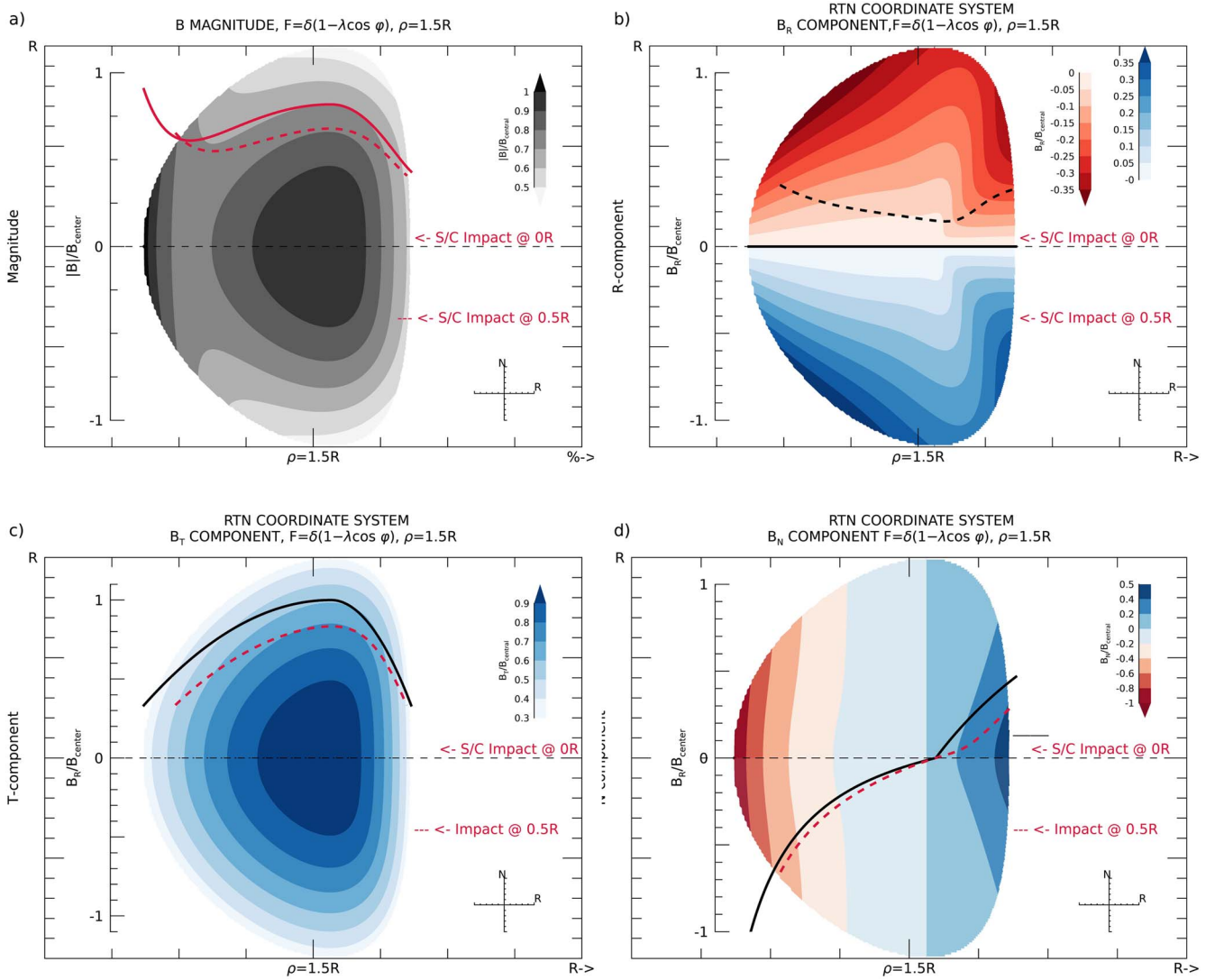


Figure 7. Contour plots of the magnetic field strength (panel (a)) and RTN components distributed on the flux rope cross section in the case of a distorted cross section with a geometry of $F = \delta(1 - \lambda \cos \varphi)$ with $\rho = 1.5R$ to enhance the effect of the curvature (Figure 4(b)). Overplotted in each contour plot are the magnetic field values measured by a spacecraft crossing through the flux rope center and at a 50% radial distance from the center, $y_0 = 0.5R$ (solid and dashed lines, respectively).

Given the relative orientation of the flux rope axis to the spacecraft trajectory, the B_T component has a very similar profile to the magnetic field strength (Figures 5(c), 6(c), and 7(c)). Due to the distortion, there is a displacement of the maximum toward the distorted area, as is also observed in the magnetic field configuration (black lines). However, this component does not display any feature associated with the curvature.

The distortion is evident in the B_R component. This component is the one that provides information about the spacecraft impact distance to the center. In general, as described largely in the literature (see, for instance, Démoulin et al. 2013; Nieves-Chinchilla et al. 2018b), this component is completely flat or curved with its maximum in the center, depending on the orientation when circular axial symmetry is assumed. The contour plot in Figure 5(b) illustrates this case with a constant surface perpendicular to the cross section. Thus in this case, for the two spacecraft crossings simulated, we find constant values for the spacecraft impact at the center, with $B_R = 0$ and $B_R = \text{constant}$ in the case of $y_0 = 0.5R$. The chirality determines the sign, so in our

left-handed flux rope, the bottom half provides positive B_R values. In the case of crossing through the top half, the B_R values would be negative. As we add distortion (Figure 6(b)) or curvature (Figure 7(b)), the contours indicate a sudden change shortly after the compressed front of the cross section. This effect is illustrated with the crossing at $y_0 = 0.5R$ (black dashed line). In the case of distortion only (Figure 6(b)), B_R remains almost constant right after the front compression. However, in the case of adding curvature (Figure 7(b)), in addition to the sudden change close to the compressed area, there is an increase (in magnitude) at the back of the structure (black dashed line). Interestingly, the effects of both curvature and distortion go unnoticed in the case of spacecraft crossing through the center (black solid line) and are more noticeable as the spacecraft impact distance increases (black dashed line).

The B_N component changes polarity from north to south (Figures 5(d), 6(d), and 7(d)). For the CC geometry, the change in polarity occurs in the center of the cross section but the distortion implies a displacement toward the front of the cross section. Thus, for this specific case, the duration of the positive polarity of the B_N

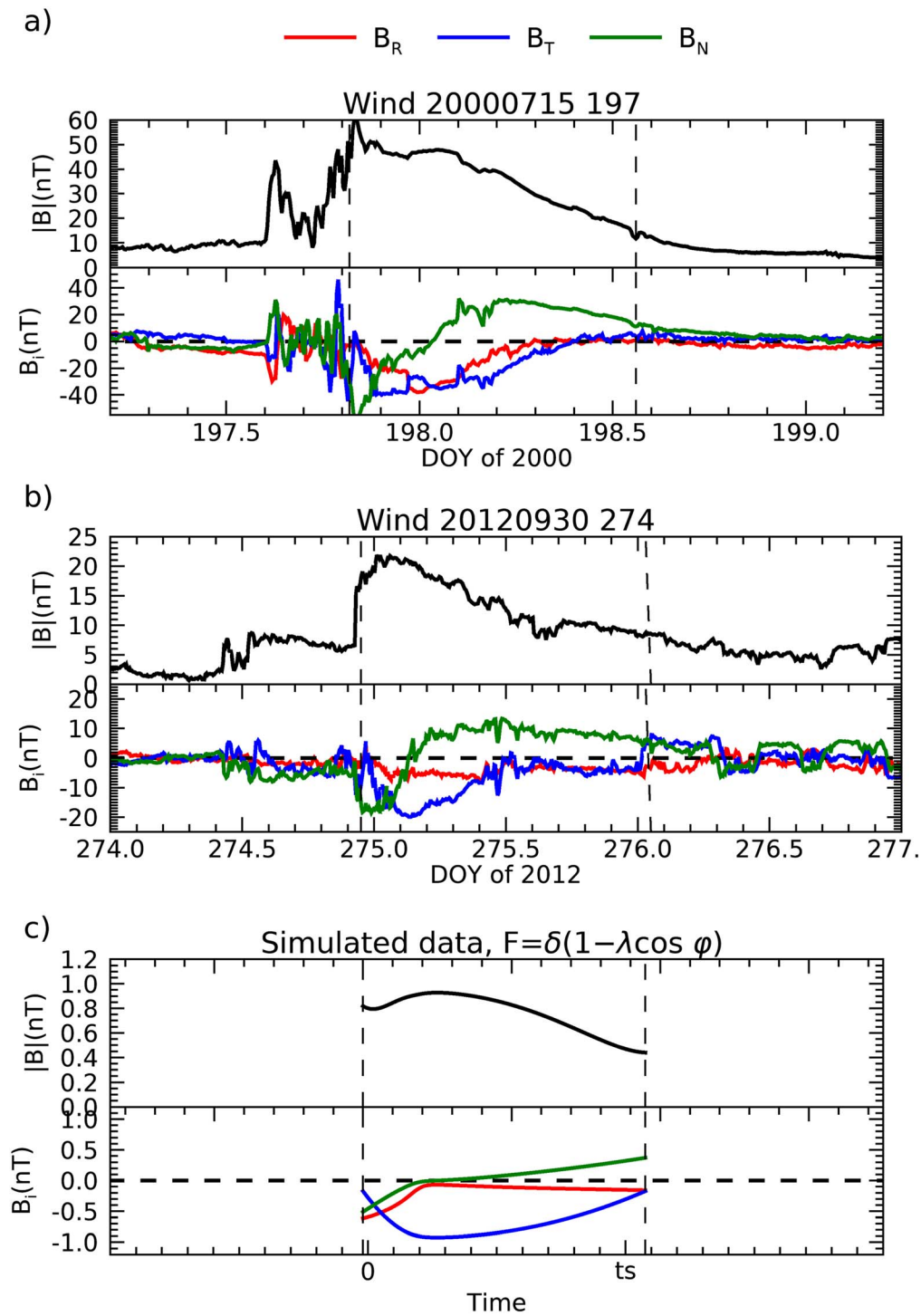


Figure 8. ICMEs observed by the Wind spacecraft and simulated data. (a) The Bastille Day event observed on 2000 July 15; (b) the event observed on 2012 September 30. The plots display the magnetic field magnitude and components in the RTN coordinate system. (c) Simulated magnetic field observations of a spacecraft crossing a distorted flux rope. The selected function can be found at the top of the plot and the parameters' values are $\rho = 2.5R$, $\tau = 1.2$, chirality = -1 , $C_{10} = 1.5$, $\lambda = 0.5$, and $\delta = 0.5$. The two vertical dashed lines indicate the magnetic obstacle boundaries.

component is almost half that of the negative polarity. The effect of the curvature implies a rapid change as the spacecraft approaches the curved area. For the flux rope orientation, the B_N component is the one that mostly contributes to the increase in the back side of the magnetic field strength. In this case, the increase of the impact distance (red dashed lines) to the center implies again a mitigation of the sudden change in polarity that is observed with distortion and curvature.

4. Brief Discussion about In Situ and Remote-sensing Observations of Distorted Structures and the Implications on Space Weather Forecasting

Figure 8 displays two ICMEs observed by the Wind spacecraft (see Wind ICME list⁴; Nieves-Chinchilla et al. 2018b). These

⁴ <https://wind.nasa.gov/ICMEindex.php>

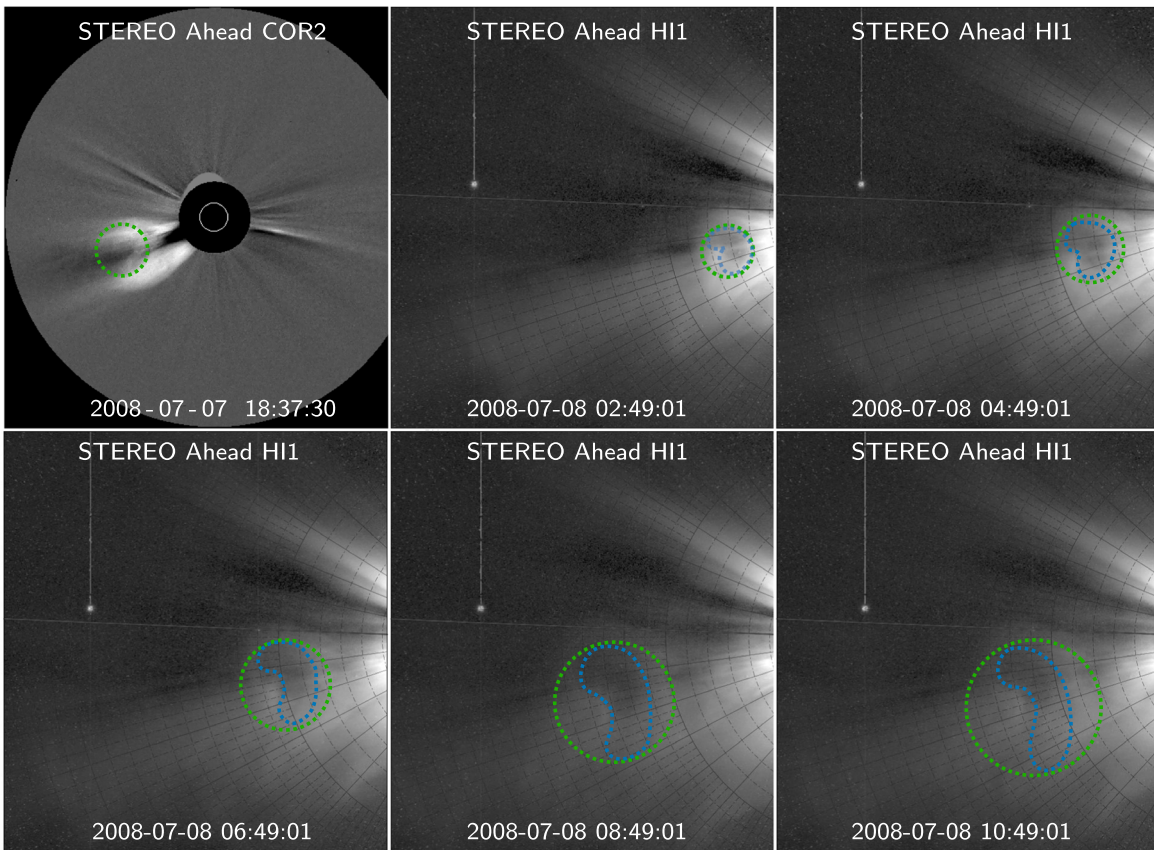


Figure 9. Flux rope CME event and its evolution in the interplanetary medium. Top left panel: The CME on 2008 July 7 as seen by the COR2-A coronagraph (field of view: $\sim 4\text{--}15$ solar radii), with the circular flux rope structure outlined by the green dotted circle. Remaining panels: The same CME on 2008 July 8, seen evolving with time by the HI1-A instrument (field of view: $\sim 15\text{--}90$ solar radii). The light blue dots outline the distorted cavity as it flattens with time, in comparison with a circular cross section.

are two examples where magnetic field signatures associated with distortions can be seen in in situ observations: at the top, the very well known Bastille Day event observed on 2000 July 15 and, at the bottom, the event observed on 2012 September 30. The plots display the magnetic field magnitude at the top and the magnetic field components in the RTN coordinate system at the bottom. The two vertical dashed lines indicate the magnetic obstacle boundaries. Based on the boundaries selected, both events display signatures associated with a flux rope, i.e., rotation of the magnetic field direction, a coherent magnetic structure, and (not shown here) association with plasma signatures. In both cases, there is a clear compression in the magnetic field strength at the front of the structure. In the case of the Bastille Day event, the B_R component displays a clear change in profile. The first part is curved to negative values and the second half rapidly reaches a zero flat value as described by Figure 7(b), in what would be a spacecraft crossing above but close to the flux rope axis in a structure highly compressed at the front. Both events display asymmetric profiles similar to those of the magnitude in the B_T component, which indicates that the structure axis is perpendicular to the spacecraft trajectory. Finally, the B_N component, in both cases, crosses the polarity from south to north very close to the front, while the positive polarity phase of the B_N component lasts almost twice as long in the case of the Bastille Day event and almost three times as long in the case of the 2012 September 30 event.

Figure 8(c) displays the simulated observations of a spacecraft crossing from the front, with a perpendicular axis, to a distorted cross section based on the function $F = \delta(1 - \lambda \cos \varphi)$. The parameters selected are $\rho = 2.5R$, $\tau = 1.2$, chirality = -1 , $C_{10} = 1.5$, $\lambda = 0.5$, and $\delta = 0.5$. Although the magnetic field components and magnitude are not identical to those of the real events, the visual comparative analysis exemplifies how this model may aid in the interpretation of actual observations exhibiting distortions. This exercise based on visual inspection, accompanied by exploration of the physical problem using machine-learning techniques (see, for instance, dos Santos et al. 2020; Narock et al. 2022), will allow us to make more accurate 3D reconstructions of the flux rope morphology, geometry, and physical parameters based on in situ observations.

Distortions not only are evident in in situ observations, but also can be distinguished remotely in white light imagery. This is the case of the CME seen on 2008 July 7 (top left panel of Figure 9) as it crosses the field of view of the STEREO/SECCHI COR2-A coronagraph. Its main axis of symmetry is approximately aligned with STEREO-A's line of sight, so that the cross section of the magnetic flux rope can be discerned in the image as circular threads outlining a dark circular cavity (indicated by the green dashed circle). The other panels of Figure 9 show the same CME as it evolves in the interplanetary medium, within the field of view of the STEREO/SECCHI HI1-A telescope. At these distances, the dark circular cavity is

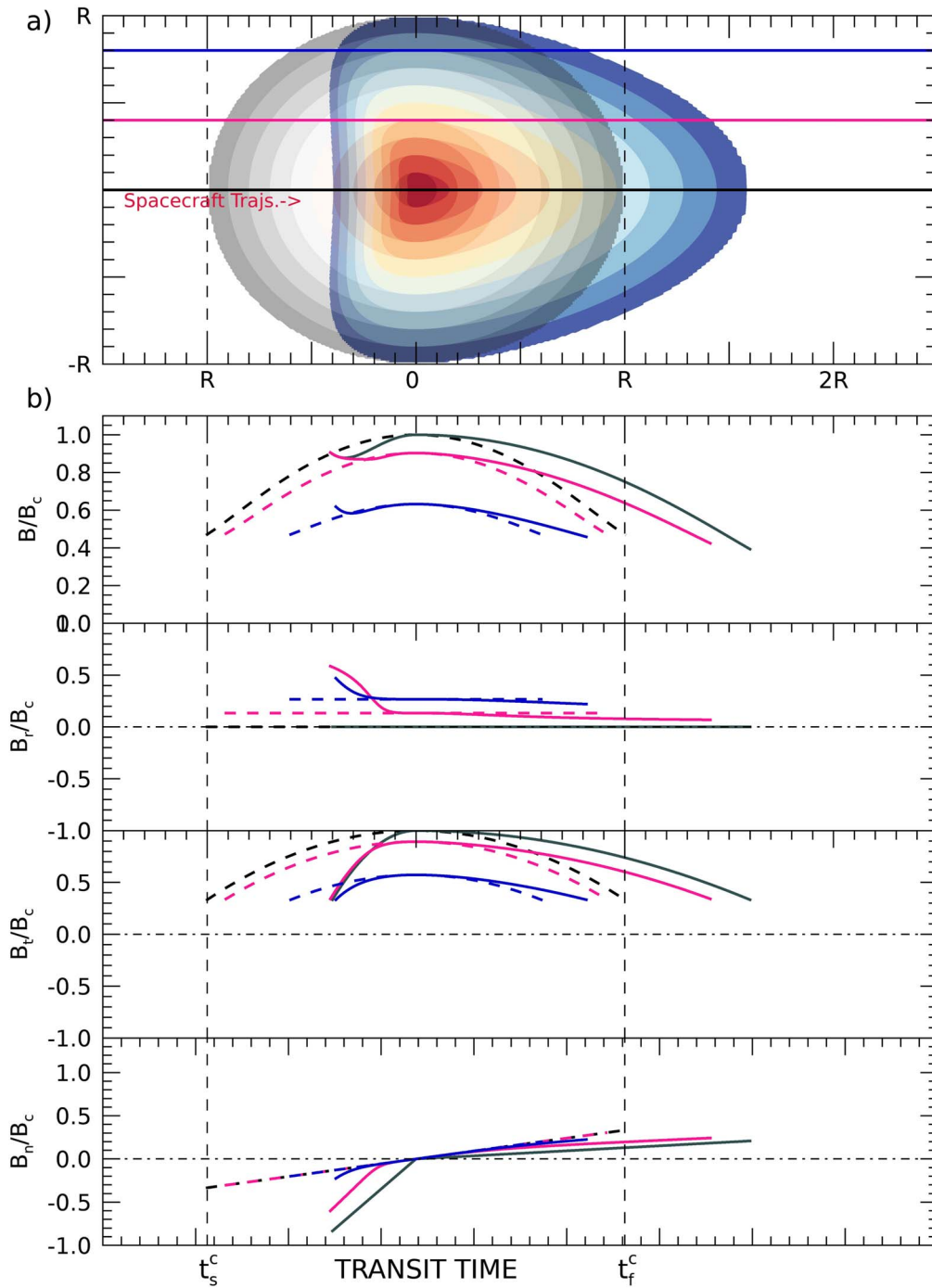


Figure 10. (a) A representation of the circular cross-section flux rope (black and white) overplotted with distorted cross sections (colored) based on the $F = \delta(1 - \lambda \cos \varphi)$ geometry. The three colored (black, red, and light blue) lines indicate a spacecraft trajectory crossing from the left. (b) Simulation of the expected in situ observations of the magnetic field magnitude and RTN components normalized to the central value (B_c) from the three spacecraft trajectories crossing a distorted and a nondistorted flux rope at different distances from the center. The vertical dashed lines connect the size of the flux rope at the top with the crossing duration along the circular flux rope center at the bottom.

distorted into a heart-shaped form (light blue dots) that flattens with distance. This case would be comparable to the one illustrated in Figure 2(d), but considerably flattened.

Figure 10 illustrates the impact of the distortion in critical elements for a reliable space weather capability such as the duration and the arrival time. At the top, Figure 10(a) displays in black and white a circular cross section and a colored distorted cross section based on the function $F = \delta(1 - \lambda \cos \varphi)$ ($\tau = 1.5$, negative chirality, $C_{10} = 2$, $\lambda = 0.6$,

and $\delta = 0.6$), where R is the radius of the circular cross section in arbitrary units. This overlaid image could represent a case of a distorted structure fitted by the conventional gradual cylindrical shell (GCS) forward-modeling technique (Thernisien et al. 2006, 2009), which is only capable of simulating structures with circular cross sections. This could be one of the options in the attempt to fit the GCS technique in actual observations, very similar to the illustration in Figure 9.

Figure 10(a) shows a three-spacecraft crossing with trajectories from the left through the center (black line), to halfway to the edge (red line), and to very close to the edge (blue line). For the example case, the maximum duration of the spacecraft within the structure will be when it crosses the center (black line) with a duration $D_c = t_f^c - t_s^c$ in the case of a circular cross section (bounded by two black dashed vertical lines) as assumed by the GCS technique. In contrast, the duration would be $D_d = t_f^d - t_s^d \sim 1.2D_c$ for the distorted case (bounded by two red dashed lines). Note that we do not use specific time units but do a relative comparison, since the duration or transit time will depend on the bulk velocity of the structure and its size (R). Note also that this analysis is conditioned by a cross-section distortion.

Figure 10(b) represents a comparative analysis of the simulated in situ magnetic field observations of a spacecraft crossing a circular (dashed line) and a distorted structure (solid line). This exercise illustrates the possible cause of being off in the prediction of the CME arrival time. By assuming a circular cross section, the GCS reconstruction is typically performed to fit the height of the distorted structure for this specific type of distortion. Then, on the basis of the GCS fit, we would make a prediction of the arrival time on the basis of the nondistorted model. For the example case, the error in the arrival time will vary depending on the spacecraft distance to the center. In the case of a crossing through the center, the flux rope impact to the spacecraft will be delayed by $\sim 30\%$, the expected duration assuming a circular cross section ($\sim 30\%D_c$). Interestingly, the peak or maximum of the magnetic field will remain in the same location since the compression will not displace the flux rope center and the location of the sign change crossing in the B_N polarity will not change. However, since the change in polarity is not displaced, the duration with negative polarity will be, at least, half shorter than expected, and the B_N positive polarity duration will be longer than predicted. Thus, the space weather quantities may be impacted by these changes in the magnetic field profiles.

Physical parameters, such as magnetic fluxes, are also relevant for space weather studies. In the case of poloidal flux, the impact of distortion on this parameter would depend on the accuracy of the fitting based on either remote-sensing or in situ observations. Thus, based on Equation (A2) in the Appendix, the poloidal magnetic flux is not impacted by distortion if the estimation of the radial size (R) of the structure is correct. In the case of toroidal magnetic flux, deviation from the actual value will depend on the integral

$$\int_0^{2\pi} \bar{g} d\varphi. \quad (48)$$

This factor will, in general, change the expected 2π value for the CC case in the case of axial or toroidal magnetic flux. For instance, in the elliptical case, Figure 2(a), the result of the integral will be to reduce the toroidal magnetic flux into the δ value of the expected or assumed CC case. This will be also the effect in the case/example that we have developed in this paper with $F(\varphi) = \delta(1 - \lambda \cos \varphi)$. In this last case, the observed asymmetry in magnetic field magnitude as well as the rapid change in B_T polarity could be confused with the effect of magnetic flux erosion (e.g., Dasso et al. 2006; Ruffenach et al. 2012, 2015; Pal et al. 2020, 2021) if the structure is modeled assuming a circular geometry. It is also very important to highlight that the analysis carried out in this section is an example that requires more in-depth examination using real

observations, ideally cases where remote-sensing and in situ observations can be synchronized.

5. Summary and Final Remarks

This paper presents an improvement to the CC and EC models (Nieves-Chinchilla et al. 2016, 2018a). Based on the mathematical formulation developed for the EC model, we have moved forward to more complex and perhaps more realistic distortions of heliospheric flux ropes. Here we have presented a model based on a toroidal geometry and expanded to a general cross-section distortion. We have illustrated the model with four functions, the morphology, and the internal magnetic field distribution in Section 2. As a proof of concept, in Section 3.2, we have developed the model with a particular cross section based on the geometry $F = \delta(1 - \lambda \cos \varphi)$.

Section 3.2 describes the in situ implications of distortion on heliospheric flux ropes. We have simulated two crossings of a spacecraft through a flux rope (at the center and halfway to the outer boundary) with two different curvatures and in comparison with a regular CC geometry. We have mapped (using contour plots) the magnetic field magnitude and the three RTN magnetic components for the three cross sections and discussed the changes in the profiles of the magnitude and components that the magnetometer would record in the two crossings and as compared with the CC geometry for two different global curvatures.

The exercise carried out in Section 3.2 provides the opportunity to identify examples in real observations. In Section 4 we have included two real events from the Wind ICME catalog (Nieves-Chinchilla et al. 2018b) with magnetic configurations that depart from the expected CC geometry. Under visual inspection, we have identified in situ signatures associated with the distortion, such as asymmetry in the magnetic field strength, different duration from what is expected from a CC geometry, and a significant difference in the duration of the magnetic field polarity transition in the spacecraft path. To assess different types of cross-section distortions and axis curvatures, exhaustive inspection of real events is required, with remote-sensing observations as a starting point.

The reconciliation between multiple observations, including heliospheric imaging, and new numerical techniques is far from successful (see, for instance, Al-Haddad et al. 2013; Wood et al. 2017). In order to develop a robust 3D physics-driven modeling and reconstruction technique, the inclusion of constraints from imaging observations in reconstruction techniques, accompanied by Monte Carlo simulations, human and machine training techniques, and eventually the evaluation of dynamics associated with distortion and deformation (Kay & Nieves-Chinchilla 2021), is a key element to take into account toward a better description of flux ropes in the heliosphere.

The work of T.N.-C. is supported by the National Aeronautics and Space Administration under grant 80NSSC19K0274 issued through the Heliophysics Guest Investigators Program, the Heliophysics Internal Funds (HIF), the STEREO mission, and Solar Orbiter mission. H.C. is a member of ‘‘Carrera del Investigador Científico’’ of CONICET, and is supported by projects MSTCA-ME0008181TC (UTN) and 11220200102710CO (CONICET). We acknowledge use of data from the STEREO (NASA) mission, produced by the SECCHI consortium. The displayed STEREO/SECCHI HI-1 images are a Level-2 product from the Southwest Research Institute in Boulder, Colorado.

Appendix

Similar to those in previous papers, the relevant physical quantities to study these structures in heliophysics can be obtained from previous equations. Below we list some of them, such as those for magnetic fluxes,

$$\begin{aligned}\Phi_\psi &= \int B_c^\psi dA_\psi = \int B_c^\psi g^{1/2} dr d\varphi \\ &= \mu_0 \int_0^\varphi \bar{g} d\varphi \int_0^R r f(r) \Big|_0^r dr\end{aligned}\quad (\text{A1})$$

$$\Phi_\varphi = \int B_c^\varphi dA_\varphi = \int B_c^\varphi g^{1/2} dr d\psi = 2\pi\mu_0 \int_0^R rk(r) dr. \quad (\text{A2})$$

Obviously, the toroidal magnetic field will depend on the cross-section geometry, while the poloidal magnetic flux is not altered.

The magnetic energy is

$$W = \int \frac{B^2}{2\mu_0} dV = \int \frac{B^2}{2\mu_0} g^{1/2} dr d\psi d\varphi. \quad (\text{A3})$$

For completeness we include the magnetic helicity, calculated from a dot product with the magnetic potential (see Woltjer 1958; Taylor 1974; Brown et al. 1999; Arfken & Weber 2005),

$$H = \int \mathbf{B} \cdot \mathbf{A} dV = \int g^{1/2} g_{ik} B_c^i A_c^k dr d\psi d\varphi. \quad (\text{A4})$$

The vector potential also requires an additional calculation that will depend on the distortion and may also require numerical solutions.

Finally, the nonscaled covariant cross-product that will lead to the components of the Lorentz force is

$$(\mathbf{j} \times \mathbf{B})|_{i,c} = g^{1/2} \epsilon_{ijk} j_c^j B_c^k. \quad (\text{A5})$$

Expanding the equation, now there are toroidal and poloidal components in the internal Lorentz forces due to the distortion and curvature:

$$(\mathbf{j} \times \mathbf{B})|_{c,r} = rh_\psi \bar{g} (j_c^\psi B_c^\varphi - j_c^\varphi B_c^\psi) \quad (\text{A6})$$

$$(\mathbf{j} \times \mathbf{B})|_{c,\psi} = -rh_\psi \bar{g} (j_c^r B_c^\varphi) \quad (\text{A7})$$

$$(\mathbf{j} \times \mathbf{B})|_{c,\varphi} = rh_\psi \bar{g} (j_c^r B_c^\psi). \quad (\text{A8})$$

This model establishes a mathematical formulation to explore distortions in observed 3D flux ropes, but the solution of the above equation system would change depending on the

kind of distortion of the flux rope under study as well as on the internal distribution of current densities. Following the approach in Nieves-Chinchilla et al. (2016, 2018a), we evaluate the solutions to the equations based on the general radial variation of the current densities with a specific geometry based on $F = \delta(1 - \lambda \cos \varphi)$ for a highly curved and cylindrical flux rope.

ORCID iDs

Teresa Nieves-Chinchilla  <https://orcid.org/0000-0003-0565-4890>

Miguel Angel Hidalgo  <https://orcid.org/0000-0003-1617-2037>

Hebe Cremades  <https://orcid.org/0000-0001-7080-2664>

References

- Al-Haddad, N., Nieves-Chinchilla, T., Savani, N. P., et al. 2013, *SoPh*, **284**, 129
- Arfken, G. B., & Weber, H. J. 2005, *Mathematical Methods for Physicists* (6th ed.; Amsterdam: Elsevier)
- Brown, M. R., Canfield, R. C., & Pevtsov, A. A. 1999, *Magnetic Helicity in Space and Laboratory Plasmas*, Vol. 111 (Washington, DC: AGU), doi:10.1029/GM111
- Burlaga, L., Sittler, E., Mariani, F., & Schwenn, R. 1981, *JGR*, **86**, 6673
- Dasso, S., Mandrini, C. H., Démoulin, P., & Luoni, M. L. 2006, *A&A*, **455**, 349
- Démoulin, P., Dasso, S., & Janvier, M. 2013, *A&A*, **550**, A3
- Domingo, V., Fleck, B., & Poland, A. I. 1995, *SoPh*, **162**, 1
- dos Santos, L. F. G., Narock, A., Nieves-Chinchilla, T., Nunez, M., & Kirk, M. 2020, *SoPh*, **295**, 131
- Fox, N. J., Velli, M. C., Bale, S. D., et al. 2016, *SSRv*, **204**, 7
- Hau, L.-N., & Sonnerup, B. U. Ö. 1999, *JGR*, **104**, 6899
- Hidalgo, M. A., Cid, C., Vinas, A. F., & Sequeiros, J. 2002a, *JGRA*, **107**, 1002
- Hidalgo, M. A., Nieves-Chinchilla, T., & Cid, C. 2002b, *GeoRL*, **29**, 1637
- Hu, Q. 2017, *ScChD*, **60**, 1466
- Kaiser, M. L., Kucera, T. A., Davila, J. M., et al. 2008, *SSRv*, **136**, 5
- Kay, C., & Nieves-Chinchilla, T. 2021, *JGRA*, **126**, e2020JA028911
- Kilpua, E., Koskinen, H. E. J., & Pulkkinen, T. I. 2017, *LRSF*, **14**, 5
- Lepping, R. P., Jones, J. A., & Burlaga, L. F. 1990, *JGR*, **95**, 11957
- Lundquist, S. 1951, *PhRv*, **83**, 307
- Müller, D., St. Cyr, O. C., Zouganelis, I., et al. 2020, *A&A*, **642**, A1
- Narock, T., Narock, A., Dos Santos, L. F. G., & Nieves-Chinchilla, T. 2022, *FrASS*, **9**, 838442
- Nieves-Chinchilla, T., Jian, L. K., Balmaceda, L., et al. 2019, *SoPh*, **294**, 89
- Nieves-Chinchilla, T., Linton, M. G., Hidalgo, M. A., et al. 2016, *ApJ*, **823**, 27
- Nieves-Chinchilla, T., Linton, M. G., Hidalgo, M. A., & Vourlidas, A. 2018a, *ApJ*, **861**, 139
- Nieves-Chinchilla, T., Vourlidas, A., Raymond, J. C., et al. 2018b, *SoPh*, **293**, 25
- Pal, S., Dash, S., & Nandy, D. 2020, *GeoRL*, **47**, e2019GL086372
- Pal, S., Kilpua, E., Good, S., Pomoell, J., & Price, D. J. 2021, *A&A*, **650**, A176
- Pesnell, W. D., Thompson, B. J., & Chamberlin, P. C. 2012, *SoPh*, **275**, 3
- Rouillard, A. P. 2011, *JASTP*, **73**, 1201
- Ruffenach, A., Lavraud, B., Farrugia, C. J., et al. 2015, *JGRA*, **120**, 43
- Ruffenach, A., Lavraud, B., Owens, M. J., et al. 2012, *JGRA*, **117**, A09101
- Sonnerup, B. U. Ö., & Guo, M. 1996, *GeoRL*, **23**, 3679
- Suess, S. T. 1988, *JGR*, **93**, 5437
- Taylor, J. B. 1974, *PhRvL*, **33**, 1139
- Thernisien, A., Vourlidas, A., & Howard, R. A. 2009, *SoPh*, **256**, 111
- Thernisien, A. F. R., Howard, R. A., & Vourlidas, A. 2006, *ApJ*, **652**, 763
- Woltjer, L. 1958, *PNAS*, **44**, 489
- Wood, B. E., Wu, C.-C., Lepping, R. P., et al. 2017, *ApJS*, **229**, 29